A MODEL AND METHODS FOR REGIONAL TRAVEL-TIME CALCULATION

Stephen C. Myers[1], Michael L. Begnaud[2], Sanford Ballard[3], Michael E. Pasyanos[1], W. Scott Phillips[2], Abelardo L. Ramirez[1], Michael S. Antolik[5], Kevin D. Hutchenson[5], Gregory S. Wagner[5], John J. Dwyer[4], and Charlotte A. Rowe[2]

Lawrence Livermore National Laboratory[1], Los Alamos National Laboratory[2], Sandia National Laboratories[3], Air Force Technical Applications Center[4], and Quantum Technology Sciences, Inc.[5]

Sponsored by the National Nuclear Security Administration

Award Nos. DE-AC52-07NA27344[1], DE-AC52-06NA253963[2], DE-AC04-94AL8500[3], and FA8620-05-C-4301[5]

ABSTRACT

This project develops a model and methods for routine computation of regional seismic travel times (RSTT) for crustal events anywhere on the globe. To improve on existing methods, the travel-time calculations must capture the effect of the 3-dimensional earth, yet the computation must be exceedingly efficient. We achieve global coverage by defining a seamless global tessellation of nodes with spacing of approximately 1°. Three-dimensional crustal structure is captured by interpolating *P*- and *S*-velocity depth profiles at each node. Mantle structure is approximated by a linear velocity gradient (as a function of depth) at each node. The linear gradient parameterization in the mantle enables an analytical approximation for the diving *Pn*/Sn ray that allows computation of travel-times in approximately 1 millisecond. Regional *Pg* and Lg propagation are approximated with a ray traveling horizontally along a mid-crustal layer. At local distance, *P* and *S* travel times are computed using the layered velocity structure under the station.

In the last year we have refined the model using a tomographic formulation that adjusts mantle velocity at the Moho, mantle velocity gradient, and a bulk crustal velocity. We used summary rays derived from ~500,000 *Pn* arrivals throughout Eurasia and North Africa in the inversion. Ten percent of the tomography data were randomly selected and set aside for testing purposes. Across Eurasia and North Africa travel time residual variance for the validation data is reduced by 32%. Based on a geographically distributed set of validation events with epicenter accuracy of 5 km or better, epicenter error using 16 *Pn* arrivals is reduced by 46% from 17.3 km (*ak135* model) to 9.3 km after tomography. Epicenter uncertainty ellipses are validated and found to contain the expected number of ground-truth epicenters within expected variations. Relative to the *ak135* model, median uncertainty ellipse area is reduced by 68% from 3070 km^2 to 994 km^2, and the number of ellipses with area less than 1000 km^2, which is the area allowed for onsite inspection under the Comprehensive Nuclear-Test-Ban Treaty (CTBT), is increased from 0% to 51%. We are currently extending the tomographic formulation and data set to include *Pg*, *Sn*, and *Lg* phases.

OBJECTIVES

This project produces a laterally variable velocity model of the crust and upper mantle that is specifically designed to compute travel times for use in routine seismic location. Because the model is limited to the crust and upper mantle, the model and methods are applicable at regional distances and we refer to the project as the RSTT model/method. The RSTT method must return the following:

1. An accurate travel-time prediction.
2. An uncertainty estimate of the travel-time prediction error.

Because the RSTT is meant for use in routine location algorithms where networks can be dynamic and precomputation of travel times for all available data may not be possible, the RSTT must also do the following:

3. Compute the travel time on-the-fly, given regional- or local-distance station/event coordinates.
4. Return the travel time in milliseconds, thus enabling the estimation of a location in a few seconds.

We have compiled an *a priori* model of the crust and upper mantle, and we improve this model using a ground-truth dataset and a tomographic technique that is tailored to optimize model parameters that are important for accurate travel time prediction. Last, we use rigorous statistical tests to measure the improvement in both travel time prediction and epicenter accuracy.

RESEARCH ACCOMPLISHED

We meet the objectives outlined above by constructing one earth model that is used in the computation of all four regional phases. Further, we adapt several approaches for regional travel-time calculation into one software package that provides a convenient travel-time calculation utility for use in seismic location and other applications that require a fast and accurate calculation for crustal seismic events. In this paper, we report on *Pn* tomography results and validation testing. We also report on preliminary *Sn* tomography results, where the starting model is derived from the *Pn* tomography result.

Model Parameterization

The RSTT model parameterization is described in previous Monitoring Research Review papers (Myers et al., 2007, 2008), and we give a brief description here. We combine the laterally variable layer approach of Pasyanos et al. (2004) with the linear mantle gradient of Zhao and Xie (1993). Velocity vs. depth profiles are defined at nodes, and the profiles at the nodes are interpolated using an efficient code developed at Sandia National Laboratories (SNL) to determine velocity at any arbitrary location (lat,lon,depth). SNL has also developed a tessellation node structure on a spheroid with node spacing of approximately 1° (Figure 1). At present, the model development domain is Eurasia and North Africa, and nodes inside that domain capture the effects of 3D structure on travel times. Outside of the development domain nodes are set to a default velocity profile based on iasp91 (Kennett and Engdahl, 1991). We also have a version of the model that is CRUST2.0 (Bassin et al., 2000) with iasp91 in the mantle and core for the region outside of Eurasia and North Africa. This parameterization provides a seamless and extensible model. Expansion beyond Eurasia and North Africa does not require a change in the model parameterization itself, only modification of the velocity structure at previously defined nodes. Further, SNL has incorporated the GRS80 ellipsoid into the model, eliminating the need for the conventional ellipticity correction to travel time predictions.

Travel-Time Calculation, *Pn* and *Sn*

Travel time computation is described in detail in previous Monitoring Research Review papers (Myers et al., 2007, 2008). The travel-time calculation is based on the method described in Zhao (1993) and Zhao and Xie (1993). This calculation is similar to the widely used approach of Hearn (1984), with an additional term (γ) introduced to account for diving rays that may occur due to a positive velocity gradient with depth and Earth sphericity.

The travel-time calculation is

$$TT = \sum_{i=1}^{N} d_i s_i + \alpha + \beta + \gamma \quad (1)$$

where *d* and *s* are the distance and slowness (taken as 1/velocity in the upper mantle) in each of the *i* segments comprising the great-circle path between Moho pierce points near the event and station, α and β are the crustal travel times at the source and receiver, and γ is a term that accounts for the effect of both mantle velocity gradient and earth sphericity. We define α as the travel time for a crustal ray at the event. Similarly, β is the travel time along a ray from the Moho to the recording station (see Myers et al., 2007, 2008 for details).

Per Zhao and Xie (1993),

$$\gamma = -\frac{c^2 Xm^3}{24 V_0} \quad (2)$$

where X_m is the horizontal distance traveled in the mantle, c is a velocity gradient in the mantle that is normalized by the velocity at the crust mantle boundary plus an additional term to account for Earth sphericity (Helmberger, 1973), and V_0 is a regional average of *Pn* velocity over the entire study area.

We introduce spatially varying *c* into the model (Phillips et al., 2007), and we calculate γ by averaging c along each ray. V_0 remains an average *Pn* velocity over the whole model, which allows us to take advantage of linear tomographic inversion methods. Tests suggest that the approximation to V_0 introduces negligible travel time error given *Pn* velocities ranging from 7.5 km/s to 8.3 km/s.

Dataset

We combine bulletin data from the International Seismological Centre, U.S Geological Survey National Earthquake Information Center, and numerous regional networks across Eurasia into a reconciled database (Flanagan et al, 2009 and references therein). To this database we have added tens of thousands of arrival-time measurements made at Lawrence Livermore and Los Alamos National Laboratories, as well as numerous detailed studies of event location. Epicenter accuracy for each event in the reconciled bulletin has been assessed using the network coverage criteria of Bondar et al. (2004). We further add non-seismic constraints based on known explosion locations, ground displacement from interferometric synthetic aperture radar (InSAR), as well as satellite imagery of man-made seismic sources. In order to diminish the possibility of introducing travel times for phases that interact with velocity discontinuities at ~410 km and ~660 km, the maximum event-station distance range is set to 15°. The minimum event-station distance range is determined by the post-critical refraction for a wave interacting with the Moho. In practice, the minimum distance varies from tens of km in the ocean (thin crust) to over 200 km in the Himalayas (thick crust).

Because the goal of this work is to produce a model for *Pn* travel time-prediction for real-time monitoring, it is important that *Pn* prediction error is unbiased relative to teleseismic *P*-wave prediction error. Previous efforts have achieved unbiased *Pn* error by using an *ad hoc* travel time correction (Yang et al., 2004). To achieve unbiased *Pn* error, we recomputed each event origin time in the tomography data using at least 10 *P*-wave arrivals. The hypocenter is then fixed during the tomographic procedure, which forces *Pn* prediction error to be unbiased relative to teleseismic *P*-wave error.

All picks are evaluated against an uncertainty budget that accounts for event mislocation, a global average of *ak135* prediction uncertainty, and arrival-time measurement uncertainty. We map the epicenter accuracy estimates to travel time uncertainty using the formulation of Myers (2001).

$$\sigma_{\text{tepi}} = \frac{\partial t}{\partial \Delta} \frac{\sigma_{\text{epi}}}{2} \quad [3]$$

where σ_{tepi} (seconds) is the standard deviation of travel time uncertainty attributable to epicenter uncertainty, σ_{epi} (km) is the 1-σ confidence in the epicenter accuracy and $\partial t/\partial \Delta$ is the phase slowness (s/km). The factor of 2 accounts for a mislocation with vector magnitude distributed Gaussian and random vector direction. The total uncertainty for a given arrival time datum is the sum of uncertainty variance for event location, model-based travel time uncertainty (e.g., Flanagan et al., 2007) and arrival-time measurement uncertainty (σ^2_{meas}). Observations outside of the 99% confidence bounds for total uncertainty ($3\sigma_{datum}$) were removed.

$$\sigma_{\text{datum}} = \sqrt{\sigma^2_{\text{tepi}} + \sigma^2_{\text{model}} + \sigma^2_{\text{meas}}} \qquad [4]$$

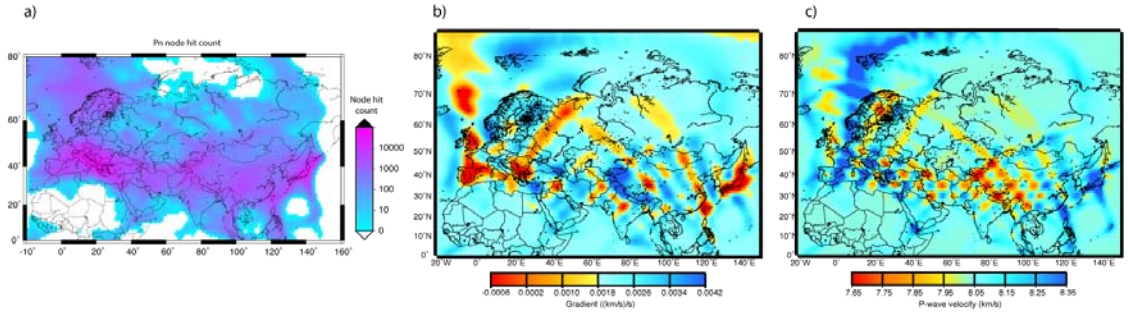

Figure 1. a) Node hit count for *Pn* rays. Nodes hit count exceeds 10,000 throughout the Tethys convergence zone and Scandinavia. Hit count varies across northern Eurasia from 10's of hits down to a few. North Africa and some ocean areas are devoid of data. b) Tomographic checkerboard test for the mantle velocity gradient (~1000 km squares). c) Tomographic checkerboard test for the mantle velocity at the Moho (~500 km squares).

In addition to data culling based on the datum-specific uncertainty budget, we also cull data based on a comparison of neighboring observations. This "local" outlier removal uses a kriging algorithm similar to the method outlined in Schultz et al. (1998). We gather all *Pn* residuals for a station and compute a geographic residual surface. The advantage of using the kriging method for interpolation is that we can also compute the point-specific uncertainty of the residual surface. Each residual is examined in the context of the station-specific residual and uncertainty surfaces and only data in the 95% confidence bounds are retained. We find that local outlier removal better identifies residuals that are due to measurement uncertainty than outlier removal based on the distribution of all residuals.

Following local outlier removal we produce summary rays for each station. Arrival time observations are again grouped by station and then evaluated at the epicenter of the associated event. For each event, we count the number of neighboring events within 0.5° (the nominal bin size), and we order events by the aforementioned count. Starting with the event having the highest count, we average residuals for all events within 0.5°, to produce a summary-ray travel time and an uncertainty estimate. Events comprising the summary ray are then discarded from the event list and the process is repeated on the event with next highest count. This process is repeated until all events for that station are exhausted. The data are reduced from ~600,000 to ~162,000 arrivals. The dramatic reduction reflects paths that are repeatedly sampled in areas with high seismicity. Reduction of the data set by summary rays not only reduces the number of data (and therefore reduces the computational expense of the tomography) by approximately 70%, but the average datum uncertainty is reduced from 1.73 seconds to 1.28 seconds. The use of summary rays also reduces sampling bias, which if left unaccounted, skews tomographic model adjustments to paths that are repeatedly sampled.

Tomography

The tomographic formulation is presented in Myers et al. (2007, 2008). In summary, we solve for the mantle velocity at the Moho, the mantle velocity gradient, and a scalar adjustment to crustal slowness at each model node. Solving for laterally variable mantle gradient is similar to the approach presented in

Phillips et al. (2007). A significant difference between the formulation presented here and more-typical *Pn*-tomography formulations is the introduction of a scalar adjustment to the slowness of the crustal stack, as opposed to a static time term to account for errors in crustal travel time. Our goal is to produce a model that improves prediction of travel time along the whole ray path, and adjusting crustal slowness better meets our goal.

Pn tomography results are presented in Figure 2. The general tectonic features that are present in the starting model are also seen in the tomographic model for mantle velocity (Figure 2a). Low-velocity anomalies in the Mediterranean region, Red Sea Rift, and Iranian Plateau remain in the RSTT model but the velocities are even lower. Mantle velocity gradient tends to be highest in convergence zones. The tomography map of mantle gradient (Figure 2b) shows a strong gradient along the Tethys convergence zone. Similarly, the mantle velocity gradient is high under the Pacific subduction zones, where the slow velocities of the wedge transition to the fast slab (See Myers et al., 2009 for further discussion).

Improvement in Travel-Time Prediction.

We leave out 10% of the tomographic data (validation data) so that non-circular tests may be performed. The validation data provides sampling across Eurasia, so residual summary statistics are a good measure of expected model performance. Recalling that origin times are determined by minimizing teleseismic *P*-wave arrival times to *ak135* predictions, it is perhaps surprising that the *Pn* error for the *ak135* model have a median value of 0.31 seconds. Median *Pn* error for the starting model is also 0.31 seconds. For the RSTT model, median *Pn* error is reduced to 0.16 seconds, a 48% reduction in median error from the *ak135* model. The Pn residual standard deviations (mean removed) relative to the *ak135*, starting model, and RSTT model are 1.99, 1.99, and 1.58 sec., respectively.

We use an interquartile measurement to compute a robust estimate of standard error for *Pn* prediction (Figure 3). Figure 3 includes the *ak135* error vs. distance curve, as well as the curve for the starting and RSTT models. The uncertainty vs. distance curve for the starting model and *ak135* are similar at near-regional distance. *ak135* uncertainty increases more rapidly with distance than the starting model in uncertainty, and the starting model uncertainty is ~0.2 seconds lower than *ak135* at far-regional distance. The RSTT model is significantly improved over both *ak135* and the starting model, with a relatively consistent error vs. distance of approximately 1.25 seconds. The RSTT model reduces error by 0.5 to 1.0 seconds compared to *ak135*. We note that a nominal 1-second measurement (pick) error variance was subtracted from the measured variance before plotting (Flanagan et al., 2007). For instance, the plotted value of 1.25 seconds (variance of 1.56 s^2) was an observed error of 1.6 seconds.

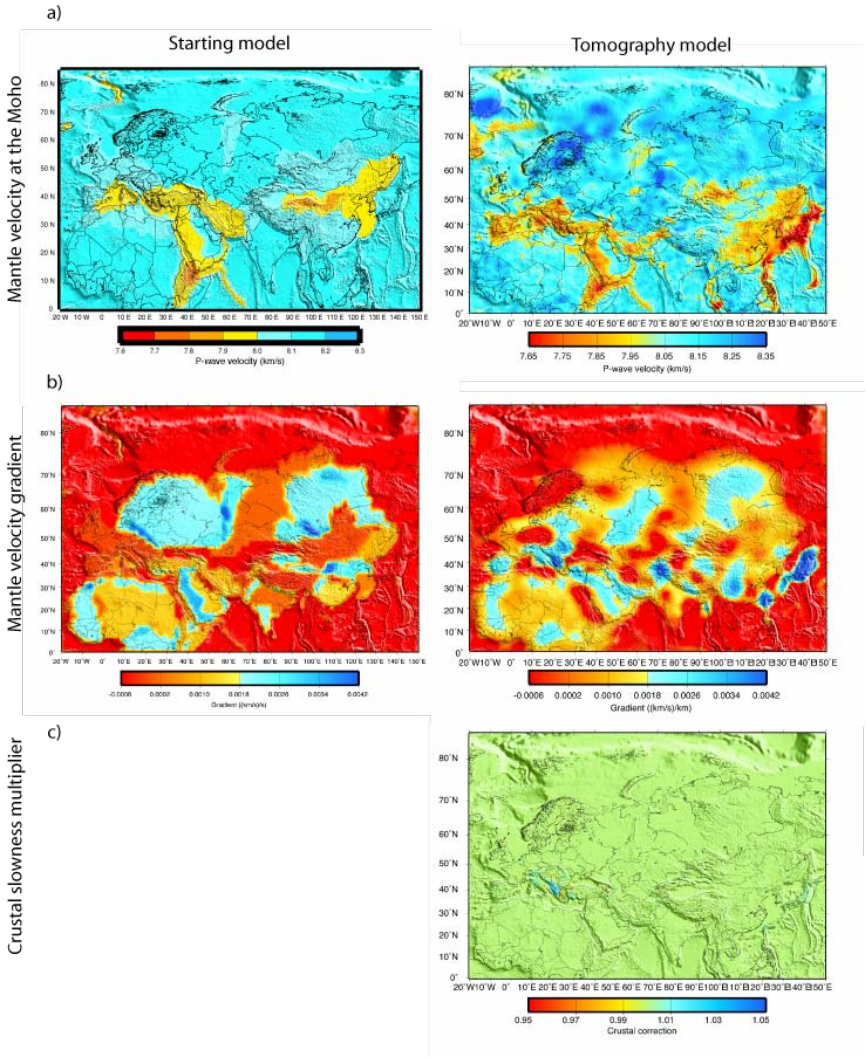

Figure 2. Comparison of starting and RSTTs. a) Velocity below the Moho. b) Mantle gradient (km/s/km). c) Scalar modification to crustal slowness.

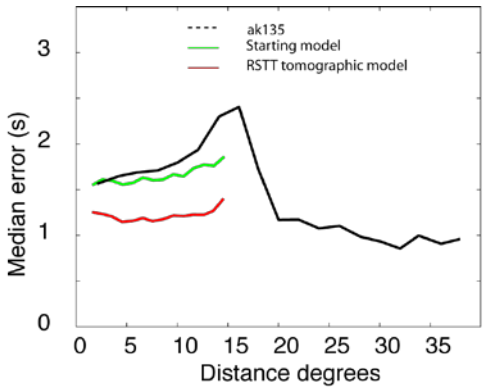

Figure 3. Travel-time error as a function of distance. The median residual in 1° distance bins is plotted for each model.

Location Tests

Figure 4 is a map of the events used in relocation tests. None of these events were used in the tomography and each of these events is either an explosion with an accurate location, or an earthquake that is surrounded by a local network (i.e., GT5 criteria of Bondar et al., 2004). These events are well distributed geographically, providing a representative sampling of location performance across the modeling region. Each event is located using *Pn* arrival times only. We use the LocOO code (Ballard, 2002), which is based on the single-event location method outlined in Jordan and Sverdrup (1981). Uncertainty ellipses were computed using the method of Evernden (1969), where "coverage" ellipse axes are scaled by *a priori* (input) model and pick uncertainties. For travel-time prediction uncertainties we use the distance-dependant curves in Figure 3, and either an analyst estimate of pick uncertainty or a nominal 1-second uncertainty. Because event depth is poorly constrained with a *Pn* data set, event depths are fixed. These events were selected partially because a large number of *Pn* arrival times are available for each event. We relocated the events using 4, 8, 16, and 32 *Pn* arrivals. Data selection was random and we created 10 realizations for each case (number of *Pn* arrivals). Results presented below are an average of the 10 realizations (See Myers et al, 2009 for details).

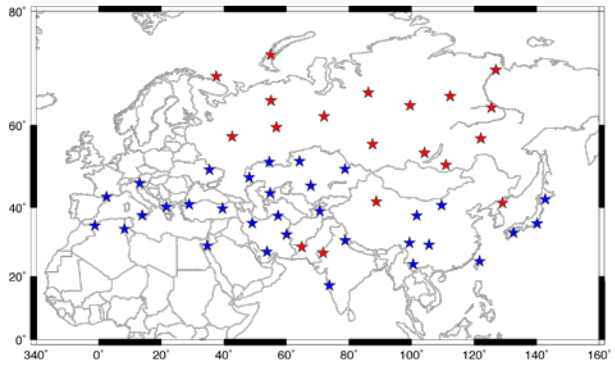

Figure 4. Validation data set used for location. The blue stars are GT5 epicenters, and the red stars are explosions with accurate epicenters.

Figure 5 summarizes epicenter error when the *ak135*, starting, and RSTT models are used for travel-time prediction in the location algorithm. Figure 5a shows that median epicenter error for the RSTT model is significantly lower than for *ak135* and the starting model, regardless of the number of *Pn* arrivals. Further, the RSTT model reaches a relatively constant level of epicenter error at ~9 km with only 8 *Pn* arrivals, whereas for *ak135* and the starting model a stable level of epicenter error at ~17 km is reached after 16 *Pn* arrivals are used.

Figure 5c summarizes ellipse area for *ak135*, the starting model, and the RSTT model, when 4, 8, 16, and 32 *Pn* arrivals are used. The primary difference between the results for the *ak135* and starting models is that there are fewer outliers that have an enormous ellipse area for the starting model than for *ak135* (i.e., the "tail" of the distribution is shorter). Ellipses for the RSTT model are consistently smaller than for the other two models. The 1000 km^2 metric (Figure 5b,c) is taken from the CTBT, which allows for an on-site inspection search area of 1000 km^2. The results show that with 4 to 8 *Pn* arrivals, none of the uncertainty ellipses are expected to be less than 1000 km^2, when either the *ak135* model or the starting model are used. Even using 32 *Pn* arrivals results in only ~23% of uncertainty ellipses with area less than 1000 km^2, when *ak135* or the starting model are used. Using the RSTT model, it is possible to achieve the 1000 km^2 goal with only 4 *Pn* arrivals, although the network configuration must be ideal. With 16 *Pn* arrivals approximately one-half of the events meet the 1000 km^2 goal, and with 32 *Pn* arrivals ~88% of ellipses meet the 1000 km^2 goal.

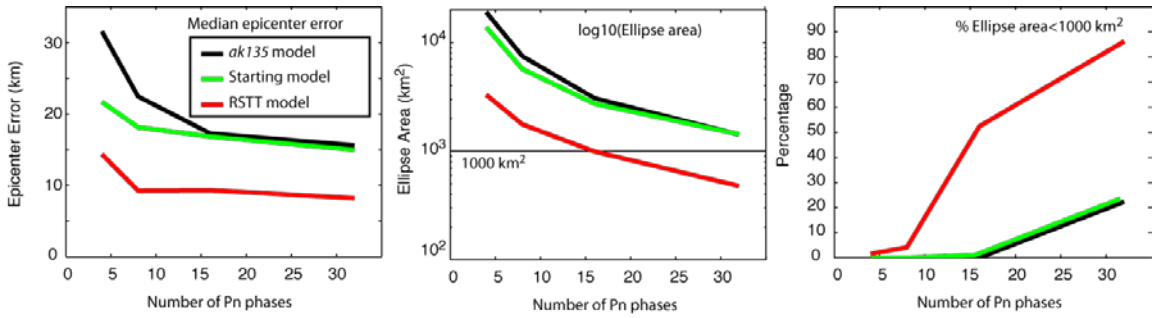

Figure 5. (a) Epicenter error, (b) semilog plot of median ellipse area, and (c) percentage of coverage ellipses with area < 1000 km^2. In (a), (b), and (c) parameters are plotted vs. number of *Pn* data used in the location. Starting model and ak135 overlap in (c).

Preliminary Results for Sn tomography.

For *Sn* tomography we first convert the *P*-wave model determined in the *Pn* tomography to an *S*-wave model. The conversion was based on the node and layer-specific *P*-wave/*S*-wave ratio (Vp/Vs) of the starting model (see above). Figure 6a shows the *S*-wave model that is derived from the *Pn* tomography model. The starting *S*-wave model is similar to the *P*-wave model presented in Figure 2, suggesting that Vp/Vs does not vary dramatically in the starting model. Figure 6b shows *Sn* coverage is good throughout Eurasia. While the *Sn* coverage is good, there is not as much *Sn* data redundancy as there is for the *Pn* data set (Figure 1). Last, Figure 6c shows the *Sn* tomography model. Changes from the starting model are modest, suggesting that the overall anomaly pattern is similar for *P* and *S* waves. The amplitudes of the anomalies are greater for the *S*-wave model, as expected.

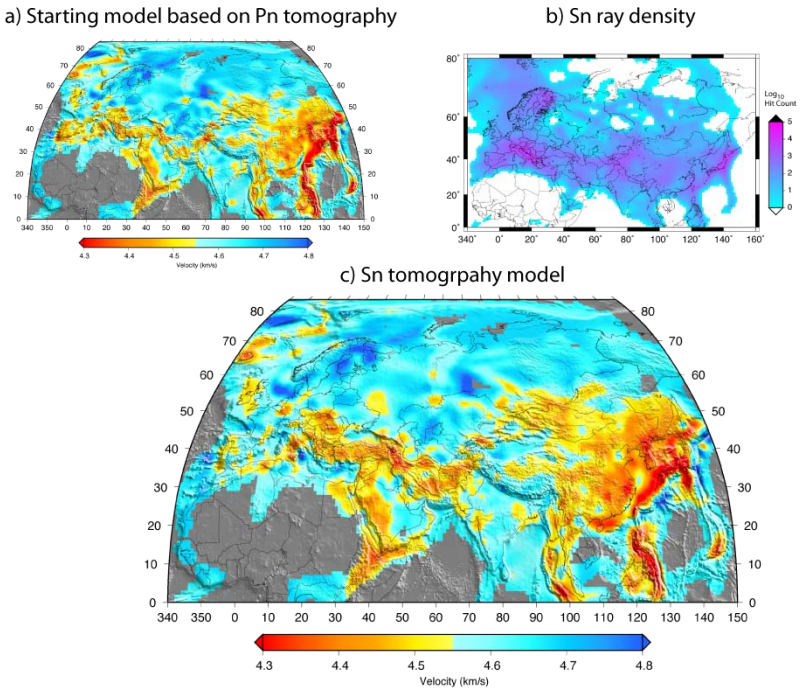

Figure 6. a) Starting *S*-wave model is derived from *Pn* tomography (see text). Upper mantle *S*-wave velocity is shown. b) *Sn* ray density. c) Preliminary upper mantle *S*-wave velocity from *Sn* tomography (see text for discussion)

CONCLUSIONS AND RECOMMENDATIONS

We describe the progress of the RSTT project to date. This project is distinct because it tailors the travel-time prediction algorithm and tomography results for use in routine seismic location algorithms. Emphasis is placed on travel-time prediction accuracy and computational efficiency of regional phases.

The tessellation model parameterization provides seamless global coverage. The use of a tessellation approach also allows fast interpolation of model parameters to extract the great-circle cross section of velocity structure that is needed to compute regional travel times. The current focus of the RSTT effort is Eurasia and North Africa, and model nodes outside of that area are set to a default velocity structure consisting of CRUST 2.0 (Bassin et al., 2000) with iasp91 for the mantle (Kennett and Engdahl, 1991). We note that the model is extensible, and a global calibration effort would entail updating node-centered velocity profiles (by whatever means), which does not require updates to the model tessellation or travel-time codes.

We make use of several approximations that result in a relatively simple algebraic form for travel-time calculations, Eq. (1). The algebraic form lends itself to a linear tomographic formulation, Eq. (8). LLNL and LANL have merged ground-truth databases to form a tomography dataset for this project. *Pn* ray coverage across Eurasia and North Africa is excellent (Figure 4). *Pn* tomographic results (Figure 5) are in general agreement with studies of the Eurasian subregions.

Across Eurasia and North Africa, travel time residual variance for the validation data is reduced by 32%. Based on a geographically distributed set of validation events with epicenter accuracy of 5 km or better, epicenter error using 16 *Pn* arrivals is reduced by 46% from 17.3 km (*ak135* model) to 9.3 km after tomography. Epicenter uncertainty ellipses are validated and found to contain the expected number of ground-truth epicenters within expected variations. Relative to the *ak135* model, median uncertainty ellipse area is reduced by 68% from 3070 km^2 to 994 km^2, and the number of ellipses with area less than 1000 km^2, which is the area allowed for onsite inspection under the Comprehensive Nuclear Test Ban Treaty, is increased from 0% to 51%.

Preliminary results for *Sn* tomography are also presented. The *S*-wave starting model is based on the *P*-wave model determined from *Pn* tomography. Conversion to *S*-waves is based on the Vp/Vs ratio of starting model at each node/layer. *Sn* and *Pn* data coverage are similar, but data redundancy is far greater for *Pn*. The *Sn* tomography model exhibits similar anomaly patterns as the *Pn* tomography model, and *Sn* anomalies are stronger when measured as a percentage of absolute velocity. The next steps in this project are to continue evaluation of S-wave inversions and to conduct validation tests on the *S*-wave model.

ACKNOWLEDGEMENTS

This project would not be possible without the full support of Leslie Casey in the Department of Energy/ NNSA Office of Nuclear Detonation Detection.

REFERENCES

Ballard, S. (2002). Seismic event location using Levenberg-Marquardt least squares inversion, Sandia National Laboratories Report, SAND2002-3083.

Bassin, C., G. Laske, and G. Masters (2000). The current limits of resolution for surface wave tomography in North America, *EOS Tran.s AGU* 81: F897.

Bondar, I., S. Myers, E. R. Engdahl, and E. Bergman, (2004). Epicenter accuracy based on seismic network criteria, *Geophys. J. Int.* 156: 483–496.

Evernden, J. F. (1969). Precision of epicenters obtained by small numbers of world wide stations, *Bull. Seismol. Soc. Am.* 59: 1365–1398.

Flanagan, M.P., S.C. Myers, and K.D. Koper (2007). Regional travel-time uncertainty and seismic location improvement using a three-dimensional a priori velocity model, *Bull. Seismol. Soc. Am*. 97: 804–825.

Hearn, T. M. (1984). *Pn* travel times in Southern California, *J. Geophys. Res*. 89: 1843–1855.

Helmberger, D. V. (1973). Numerical seismograms of long-period body waves from seventeen to forty degrees, *Bull. Seismol. Soc. Am*. 63: 633–646.

Jordan, T.H. and K.A. Sverdrup (1981). Teleseismic location techniques and their application to earthquake clusters in the south-central Pacific, *Bull. Seismol. Soc. Am*. 71: 1105–1130.

Kennett, B. L. N. and E. R. Engdahl, (1991). Traveltimes for global earthquake reference location and phase identification, *Geophys. J. Int.* 105: 429–465.

Myers, S. C. (2001). Methods of travel-time residual declustering for the Knowledge Base Calibration and Integration Tool (KBCIT), *Lawrence Livermore National Laboratory Report*, 14 pp., UCRL-ID-142521**.**

Myers, S. C., S. Ballard, C. Rowe, G. Wagner, M. Antolik, S. Phillips, A. Ramirez, M. Begnaud, M. Pasyanos, D. Dodge, M. Flanagan, K. Hutchenson, G. Barker, J. Dwyer, and D. Russell (2007). Tomography and methods of travel-time calculation for regional seismic location, in *Proceedings of the 29th Seismic Research Review: Ground-Based Nuclear Explosion Monitoring Technologies*, LA-UR-07-5613, Vol. 1, pp. 414–423.

Myers, S. C., S. Ballard, C. Rowe, G. Wagner, M. Antolik, S. Phillips, A. Ramirez, M. Begnaud, M. Pasyanos, D. Dodge, M. Flanagan, K. Hutchenson, G. Barker, J. Dwyer, and D. Russell (2008). A model and methods for regional travel-time calculation, in *Proceedings of the 29th Seismic Research Review: Ground-Based Nuclear Explosion Monitoring Technologies*, LA-UR-08-05261, Vol. 1, pp. 425–434.

Myers, S. C., S. Ballard, C. Rowe, G. Wagner, M. Antolik, S. Phillips, A. Ramirez, M. Begnaud, M. Pasyanos, D. Dodge, M. Flanagan, K. Hutchenson, G. Barker, J. Dwyer, and D. Russell (2009). Tomography and methods of travel-time calculation for regional seismic location, *Bull. Seismol. Soc. Am.*, in preparation.

Pasyanos, M. E., W. R. Walter, M. P. Flanagan, P. Goldstein, and J. Bhattacharyya (2004). Building and testing an a priori geophysical model for western Eurasia and North Africa, *Pure App. Geophys*. 161: 235–281.

Phillips, W. S., M. L. Begaud, C. A. Rowe, L. K. Steck, S. C. Myers, M. E. Pasyanos, and S. Ballard (2007). Accounting for lateral variations of the upper mantle gradient in *Pn* tomography studies, *Geophys. Res. Lett*. 34: doi:10.1029/2007GL029338.

Schultz , C.A., S. C. Myers, J. Hipp, and C. Young (1998). Nonstationary Bayesian kriging: a predictive technique to generate corrections for detection, location, and discrimination, *Bull. Seismol. Soc. Am.* 88: 1275–1288.

Yang, X., I. Bondar, J. Bhattacharyya, M. Ritzwoller, N. Shapiro, M. Antolik, G. Ekstro¨m, H. Israelsson, and K. McLaughlin (2004). Validation of regional and teleseismic travel-time models by relocating ground-truth events, *Bull. Seismol. Soc. Am*. 94; 897–919.

Zhao, L.-S. (1993). Lateral variations and azimuthal isotropy of *Pn* velocities beneath Basin and Range province, *J. Geophys. Res*. 98:109–122.

Zhao and Xie (1993). Lateral variations in compressional velocities beneath the Tibetan Plateau from *Pn* traveltime tomography, *Geophys. J. Int*. 115: 1070–1084.